WILEY | Hindawi

Research Article

Direct and Binder-Free MXene-Assisted Cobalt Manganese Phosphate Electrode Fabrication on Carbon Cloth by Electrosynthesis for Efficient Supercapacitors

Sajjad Hussain [1,2] **Pranav K. Katkar** [3] **Dhanasekaran Vikraman** [4]
Zulfqar Ali Sheikh [5] **Ghazanfar Nazir** [2] **Khalid Mujasam Batoo** [6] **Deok-Kee Kim** [5]
Hyun-Seok Kim [4] **and Jongwan Jung** [1,2]

[1]Hybrid Materials Center (HMC), Sejong University, Seoul 05006, Republic of Korea
[2]Department of Nanotechnology and Advanced Materials Engineering, Sejong University, Seoul 05006, Republic of Korea
[3]Department of Physics, Sejong University, Seoul, Republic of Korea
[4]Division of Electronics and Electrical Engineering, Dongguk University-Seoul, Seoul 04620, Republic of Korea
[5]Department of Electrical Engineering, Sejong University, Seoul 05006, Republic of Korea
[6]King Abdullah Institute for Nanotechnology, King Saud University, Riyadh 11451, Saudi Arabia

Correspondence should be addressed to Jongwan Jung; jwjung@sejong.ac.kr

In this work, MXene-assisted cobalt manganese phosphate (MXene-CMP) thin films with various Co/Mn compositions were prepared on a carbon cloth (CC) substrate via an easy and efficient low-cost electrodeposition route. MXene-CMP thin films were further used as polymer-free active materials for hybrid supercapacitors. The structural, compositional, and surface properties of the prepared MXene-CMP hybrid thin films were characterized using the latest analytical methods. The H-3 electrode exhibited enhanced specific capacitance ($840 \, F \cdot g^{-1}$ at $2 \, A \cdot g^{-1}$) with exceptional robust performance. Additionally, a symmetric H-3 MXene-CMP supercapacitor device also demonstrated a high energy density of $48 \, Wh \cdot kg^{-1}$ at $1.5 \, kW \cdot kg^{-1}$ power density and holds better cyclability (93% of its initial value after 5000 cycles). Finally, this work explored the strong potential of MXene-attached bimetallic phosphates for solving the electrochemical shortcomings of energy storage devices.

1. Introduction

To address the energy crises and power demand in the world today, the demand for high-power, environmentally friendly energy storage gadgets with high power/energy density, long life cycle firmness, and low impedance compared to batteries has increased [1, 2]. Electrochemical supercapacitor devices (SCs) are considered as outstanding candidates to achieve these requirements in various fields, such as defense, mobiles and wearable gadgets, telecommunication, road/air transportation, flexible digital electronics, and electricity grid networks [3]. Despite the significant progress on SCs, their maximum capacity, superb speed performance, and stability are insufficient to maintain high-rate operations [4, 5].

Among various electrode materials, 2D nanostructured materials, such as graphene oxide (GO), graphene, and carbon nanotube (CNT), which store charge in an electrochemical double-layer capacitors (EDLCs) mode, have attracted attention owing to the rapid response of electrolyte ions on porous carbon [6–9]. In addition, transition metal chalcogens, transition metal oxides or metal hydroxides, transitional metal carbide [10–12], transition metal phosphates (TMPs), and layered double hydroxides, which possess a pseudocapacitive charge storage behavior, have also attracted attention [13–15]. Among various 2D materials, MXene have been intensively investigated due to their intense surface and chemical properties, such as high metallic electronic conductivity (which is close to that of multilayered graphene), carrier

density (in the order of 10^{22} cm^{-3} in a vacuum), significant specific surface area, rich surface chemistry owing to the presence of large surface functionality groups (-F, –OH, and –O), pseudocapacitance, and ease of dispersion in various solvents (including water) with a high yield [6, 16, 17]. Moreover, MXene naturally exists as conductor/superconducting semiconductors or semimetals, depending on the preparation like surface termination or composition. MXene-related materials have been demonstrated as promising electrodes for supercapacitors (300–1150 F/g), owing to their tunable interlayer spacing and hydrophilicity, and for batteries, including Li–S and Li-, Na-Al-, and K-ion batteries, due to the superior conductivities, redox-active surfaces, and low diffusion barrier of metal on their surfaces [18]. Moreover, MXene provides conductive channels that prevent aggregations, facilitate swift electron transmission, and improve electrode cycle stability.

Recently, TMPs have been established to be gifted materials because of their high theoretical specific capacities, high abundance, enriched chemical stability, open/porous structural cavities, and multiple channels, as well as impressive storage capacity [19–21]. TMPs consisting of transition metals, such as Ni, Mn, and Co, are being investigated as economical active materials in the energy storage industry owing to their rich redox kinetics, reasonable rate capacitive properties, superior electrical conductivity, and remarkable cyclic performance [22, 23]. Particularly, electrochemically active TMPs, such as porous $Ni_2P_2O_7$ nanowire [24], $Mn_3(PO_4)_2$ nanosheets [25], and $Co_3(PO_4)_2$ [26], have attracted research attention for the fabrication of pseudocapacitors or battery-type materials owing to their high redox state and low cost. Binary metal-based TMPs, consisting of Co and Mn elements in the composite form, may exhibit enhanced performance than their single metallic counterparts [27]. For example, a binary metallic system consisting of Co and Mn can be considered an idyllic pseudocapacitive material due to the high oxidation potential of Co and the ability of Mn to improve the electrical characteristics of the metallic system owing to its natural abundance, excellent electron mobility, high theoretical capacitance, superior cyclic stability, and various redox chemistry with oxidation levels spanning from +2 to +7 and high energy density [28, 29]. In contrast, cobalt phosphate and manganese phosphate exhibit significant limitations, such as low electronic conductivity, poor cycling, and low specific capacitance. This indicated that cobalt phosphate and manganese phosphate could be combined to overcome their individual limitations and provided a viable solution for attaining admirable electrochemical behavior (specific capacitance and cycling). The interaction among the multimetals and consistent supply of Mn and Co atoms at high oxidation levels owing to their distinctive composition in the electrode material can be attributed to the excellent supercapacitive behavior of cobalt manganese phosphate $(Co_xMn_{3-x}(PO_4)_2$—CMP). CMP can provide remarkable electrochemical performance, such as reduced internal resistance and well-defined redox behavior. Accordingly, the decoration of bimetallic phosphates on MXene sheets has attracted attention for achieving EDLC/pseudocapacitive behavior.

In this study, MXene-assisted CMP (MXene-CMP) films with different Co and Mn contents were electrodeposited on a carbon cloth (CC) to fabricate efficient supercapacitor electrode materials. Three-electrode measurement revealed that the prepared H-3 electrode demonstrated considerably enhanced electrochemical behavior with a maximum capacitance (840 F·g^{-1} at 2 A·g^{-1}). Further, the assembled H-3-based symmetric supercapacitor device attained a high energy density of 48 Wh·kg^{-1} at a power density of 1.5 kW·kg^{-1} with an exceptional cyclability of 93% after 5000 cycles.

2. Experimental Detail

In this study, $Co_xMn_{3-x}(PO_4)_2$@MXene (H) thin films were coated on a CC substrate engaging an electrodeposition unit. First, MXene was synthesized by selectively etching of Al from Ti_3AlC_2 using an *in situ* hydrofluoric acid (HF) etchant based on the methodology described in our previous studies [30, 31]. The thin films were prepared via potentiostatic electrodeposition using the CC substrate with different ratios of Co and Mn. Thereafter, precursors $CoCl_2 \cdot 6H_2O$, $MnCl_2 \cdot 4H_2O$, and KH_2PO_4 were mixed together at various molar concentrations, as defined in Table 1, and designated as CMP and H-1, H-2, H-3, H-4, and H-5 thin films. Subsequently, 20 mg of MXene was added into the mixture to prepare MXene-based thin films (H-series), and the mixture stirring was vigorous until a transparent solution was formed. The potentiostatic deposition was performed for 15 min at a -1.1 V of constant potential. To prepare the CMP thin film, the solution was prepared without MXene using the same procedure. After the electrodeposited thin films, the as prepared films were further rinsed with deionized water to remove any loosely attached particles, after which the films were allowed to dry at room temperature. Further, the air-dried thin films were characterized, as described in the supporting information. The detailed characterization information is provided in the supporting information.

3. Results and Discussion

The electrodeposition of binary metal phosphate (CMP) and their MXene hybrids (H-series) (containing different Co and Mn compositions) on CC was achieved using potentiostatic deposition, as depicted in Figure 1. The morphological properties and composition of electrodeposited films were examined using field emission scanning electron microscope (FESEM) and energy dispersive spectroscopy (EDS), respectively. Figures S1a and b show the FESEM micrograph of the delaminated MXene sheets and their compositional profile, respectively. The microscopy image reveals the organized stacked nanosheets on the MXene structure. In addition, EDS analysis reveals the 53, 33, and 13 at.% compositions corresponding to C, Ti, and O, respectively, for the as-prepared MXene sheet. Figures 2(A) and 2(B) display the FESEM micrograph and EDS contour of electrodeposited CMP bimetallic alloy structure, respectively, which was prepared based on the molar ratio specified in Table 1. Agglomerated grains with a bundle shape are observed in the FESEM image of the CMP (composed of tiny

TABLE 1: Molar concentration of Co and Mn precursors used for the synthesis of CMP and hybrid films.

Code	MXene	$CoCl_2 \cdot 6H_2O$ (M)	$MnCl_2 \cdot 4H_2O$ (M)	KH_2PO_4 (M)
CMP	—	0.050	0.050	0.2
H-1		0.000	0.1	0.2
H-2		0.025	0.075	0.2
H-3	20 mg	0.050	0.050	0.2
H-4		0.075	0.025	0.2
H-5		0.1	0.000	0.2
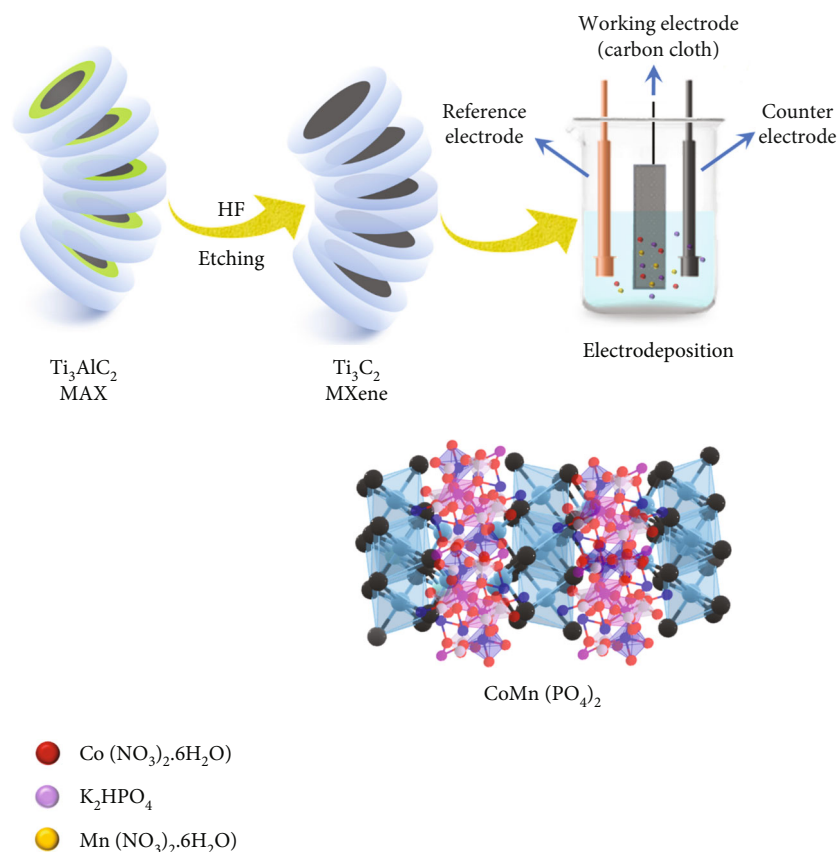
FIGURE 1: Schematic of the preparation of the MXene@CoMnPO$_4$ composite via single-step electrodeposition technique.

nanograins), which can be attributed to the coalescence process that occurred in the sample. The extracted EDS profile revealed that the CMP is composed of 31, 9, 28, and 32 at.% of O, P, Mn, and Co elements, respectively. Figure 2(C) shows the FESEM image of H-1 hybrid structures, in which MXene was electrodeposited in the absence of Co in the bath solution. The FESEM image reveals the addition of CMP particles between the MXene matrix structures. In addition, the EDS results revealed that H-1 is composed of 29, 34, 8, 17, and 12 at.% of C, O, P, Ti, and Mn elements, respectively (Figure 2(D)). Further, FESEM image reveals the presence of larger-sized agglomerated grains in the H-2 hybrid structure (Figure 2(E)), which may be attributed to the addition of 0.025 M Co into the bath solution. Consequently, the H-2 thin film exhibits a patchy-like deposition owing to the intermetallic interaction between

the bimetallic phosphates and MXene. H-2 EDS result describes the 30, 35, 7, 14, 9, and 5 at.% of C, O, P, Ti, Mn, and Co elements, respectively (Figure 2(F)). H-3 thin film FESEM image, which was prepared using equal molar concentration of Mn and Co sources, reveals the protrusion of nanowires on the agglomerated grains (Figure 2(G)), and their EDS results explore the composition of 28, 32, 8, 13, 9, and 10 at.% of C, O, P, Ti, Mn, and Co elements, respectively. These results indicated that the content of Co in the thin film increases as an increase of Co concentration. H-4 thin film FESEM image reveals the presence of well-dispersed aggregated spherical grains and protruded nanowires on their surface (Figure 2(I)). This can be ascribed to the significant decrease in the content of Mn, ensuing in a significant diminution in the formation of the agglomerated bulky grain structures. EDS of H-4 thin film explores the 29,
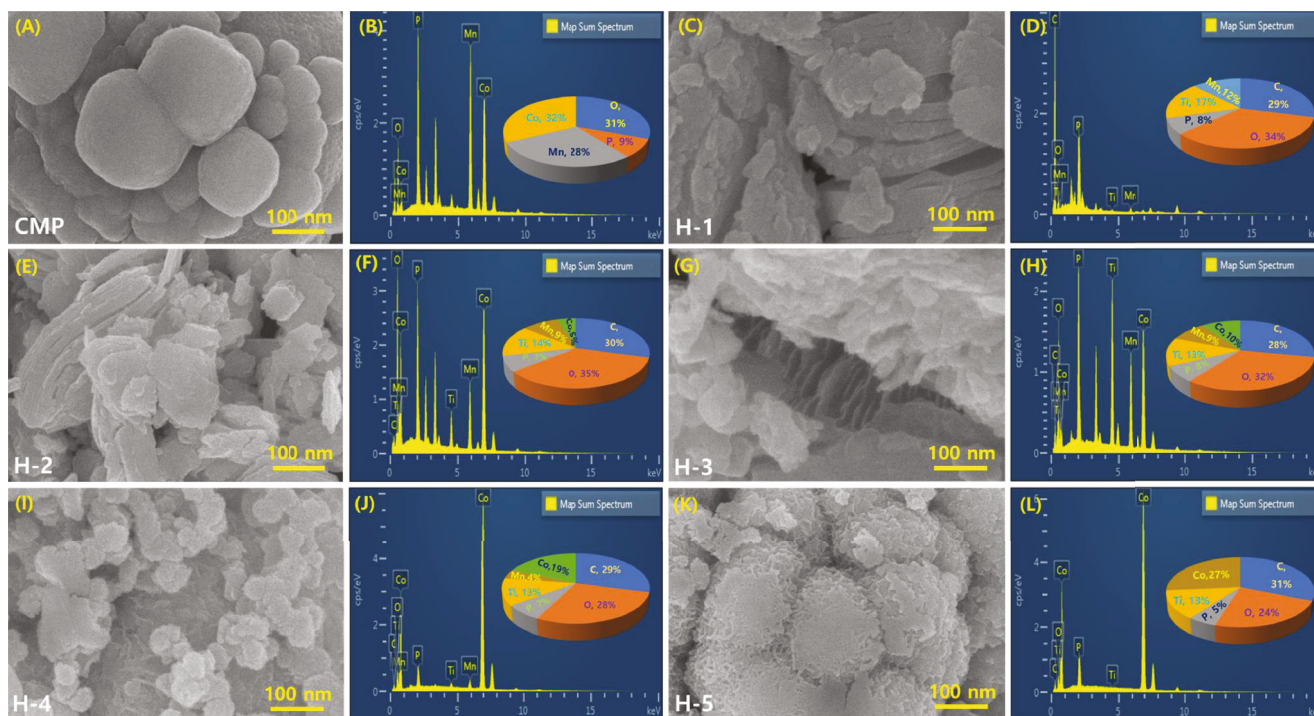
FIGURE 2: FESEM imagery of (A) CMP, (C) H-1, (E) H-2, (G) H-3, (I) H-4, and (K) H-5; energy dispersive X-ray spectroscopy (EDX) profiles of (B) CMP, (D) H-1, (F) H-2, (H) H-3, (J) H-4, and (L) H-5.
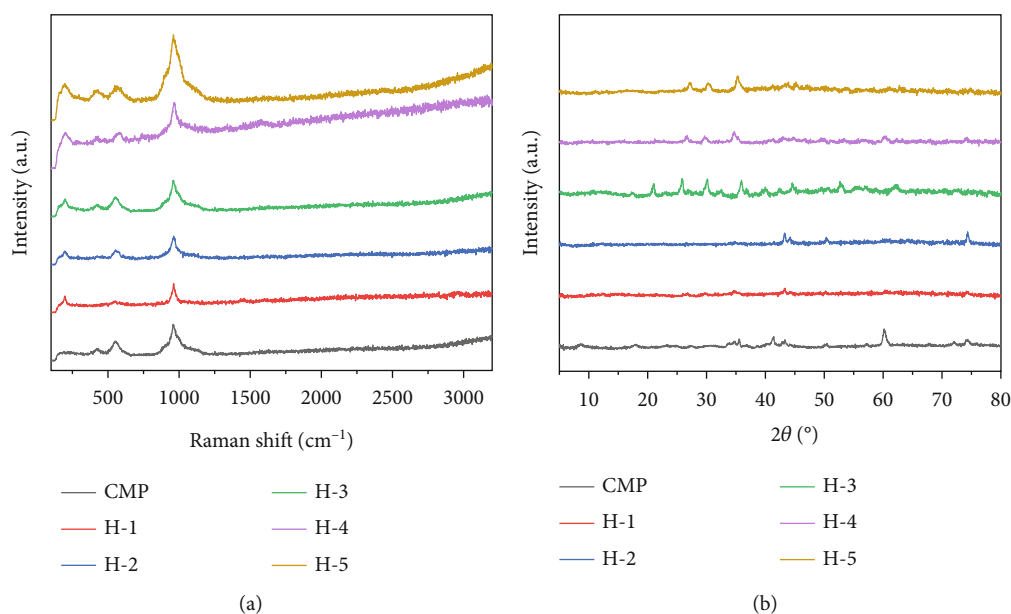

(a)

(b)

FIGURE 3: (a) The Raman and (b) XRD profiles of MXene and their composite samples.

28, 7, 13, 19, and 4 at.% of C, O, P, Ti, Co, and Mn elements, respectively (Figure 2(J)). An H-5 film FESEM image (Figure 2(K)), which was prepared with a Co source and without Mn source (as defined in Table 1), indicates the caterpillar-type surface owing to the protrusion of the characteristic cobalt phosphate nanowires on the MXene surface, with the composition of 31, 24, 5, 13, and 27 at.% for the H-5 film C, O, P, Ti, and Co elements, respectively

(Figure 2(L)). To further explore the elemental composition, elemental mapping analysis was performed on the H-3 film, which was prepared under optimized conditions. Figures S2a-g show the overall elemental mapping and the mapping of selective elements, such as Ti, C, O, Mn, Co, and P on the H-3 film, respectively. The observed mapping images strongly indicated the uniform dispersion of all the elements over the electrodeposited H-3 film.
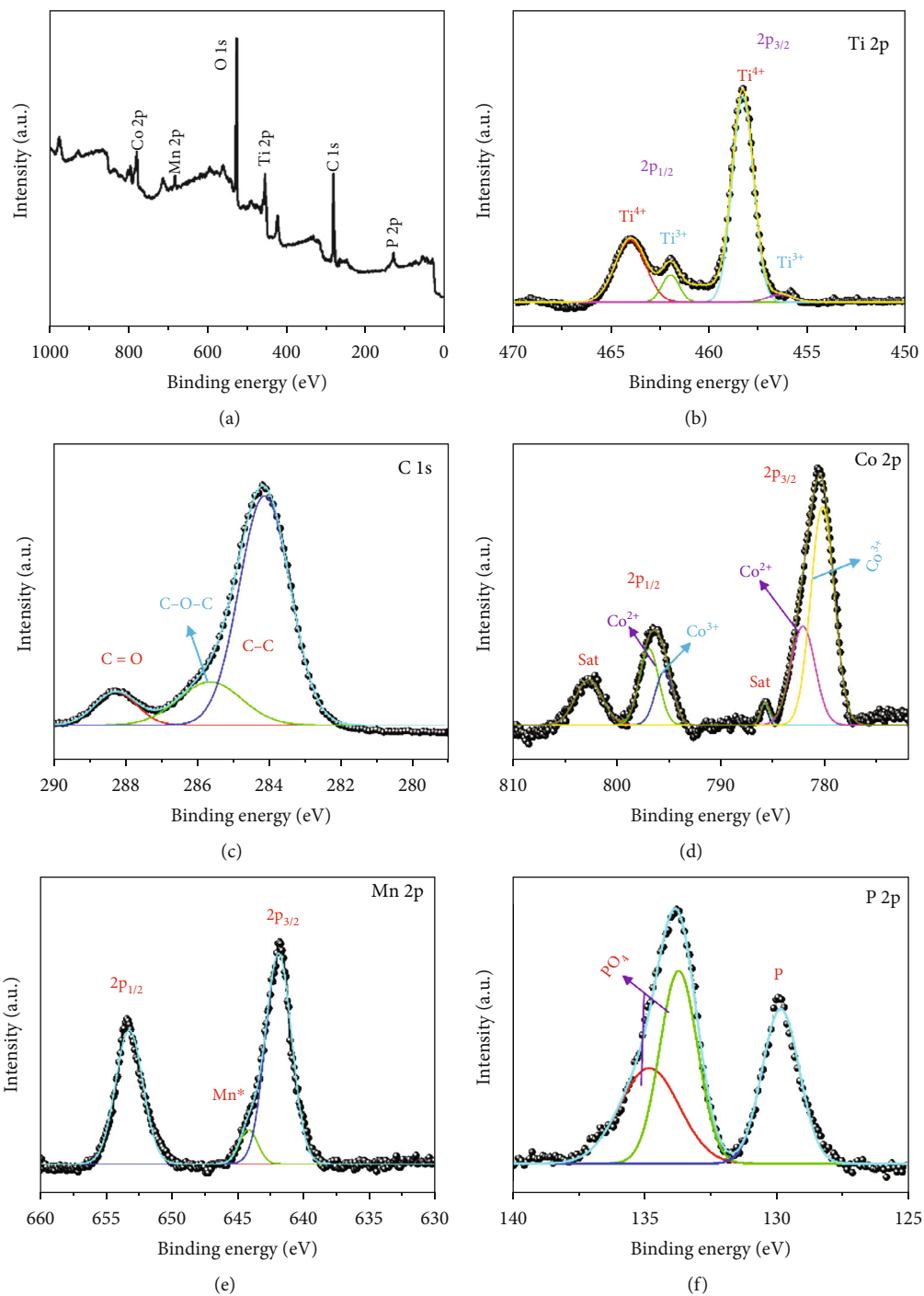
(a)

(b)

(c)

(d)

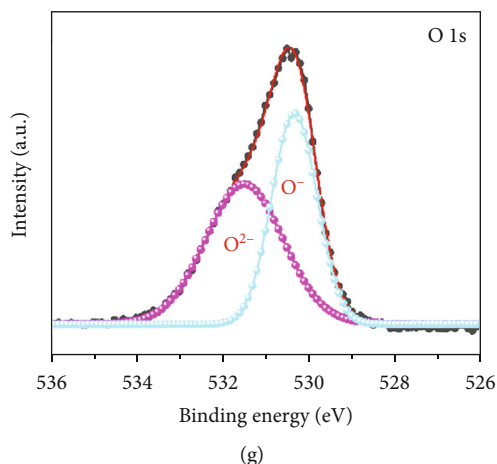(e)

(f)

FIGURE 4: Continued.

(g)

FIGURE 4: X-ray photoelectron spectra (XPS) of the hybrid H-3 sample: (a) full scan, (b) Ti 2p, (c) C 1s, (d) Co 2p, (e) Mn 2p, (f) P 2p, and (g) O 1s regions.

To confirm the structural confirmation of the electrodeposited thin films, the Raman profiles of the as-prepared CMP and H-series thin films were obtained. Figure 3(a) shows the Raman lines of the CMP and H-series films. Peaks are observed at 204, 392, 619, and $722\,cm^{-1}$ in the Raman profile of the as-prepared MXene, which corresponded to the formation of MXene (Figure S3) [30, 32]. A strong band is observed around $960\,cm^{-1}$ in the Raman spectrum of the pure CMP film (Figure 3(a)), which is credited to the ν_1 stretching mode of the phosphate ion ($\nu_1\ PO_4^{3}$) [33]. In addition, low-intensity peaks associated with the presence of Mn–Co composite were observed in the Raman profile around 199 and $530\,cm^{-1}$ [34, 35]. A strong phosphate peak is observed in the Raman profiles of the H-series hybrid films (Figure 3(a)), which attributed to their dominant presence in the prepared thin films. Moreover, strong MXene-related peaks are observed in the Raman profiles of these films, confirming the prominent influence in the resulting H-series structure. Figure 3(b) shows the X-ray diffraction (XRD) profiles of CMP and H-series films. The observed XRD profiles elucidate the semicrystalline nature due to their low amount of loading and CC substrate. In addition, the pure CMP film induces the (2-1-16), (4-2-20), (40-48), (4-1-32), and (6-1-55) lattice peaks (#771641). H-1 and H-2 composites induce a very weak crystalline profile due to the absence or low Co element in the resulting composites. Further, H-3 produces significant intense semicrystalline behavior due to the equiratio metal element integration in the composites.

To further evaluate the composition of the electrodeposited film prepared under optimum conditions (i.e., H-3 film), X-ray photoelectron spectroscopy (XPS) examination was done. Figure 4(a) shows the XPS wide region scan of H-3 film. All the element peaks are clearly indicated in the resulted profile which ascertains the H-3 composite formation. Figure 4(b) spectacles the Ti 2p spectrum of the prepared H-3 film. The swellings agreeing to the $2p_{3/2}$ and $2p_{1/2}$ spin–orbit doublets were observed at 455.8/461.9 and 459.9/465.3 eV owing to Ti^{3+}/Ti^{4+}, respectively, which corresponded to the formation of Ti–C and mixed carboxides

(TiC_xO_y) bands [36, 37]. In addition, peaks corresponding to the existence of C=O (288.3 eV), C–O–C (285.4 eV), and C–C (284.7 eV) were observed in the C 1s band (Figure 4(c)) [12]. Figure 4(d) shows the Co 2p XPS profiles. The presence of multiple spin-orbital doublets due to the Co^{2+}, Co^{3+}, and satellite peaks was detected in the deconvoluted profile, signifying the occurrence of a multivalent interaction in the resulting hybrid material [38, 39]. Mn $2p_{3/2}$ and Mn $2p_{1/2}$ peaks were obtained in the deconvoluted Mn 2p spectrum at 641.8 and 653.2 eV, respectively, along with a satellite (*) peak (Figure 4(e)) [38]. Two primary peaks, which could be attributed to the presence of phosphate ions, and a strong peak corresponding to the presence of the phosphide ion in the resulting material, were observed in the P 2p spectrum (Figure 4(f)) [40]. Figure 4(g) shows the O 1s XPS spectrum of H-3 which reveals the peaks at 530.3 eV and 531.6 eV owing to the oxygen defects (O^{2-}) and O^- (lattice oxygen), respectively [41, 42]. These results strongly confirmed the formation of $Co_xMn_{3-x}(PO_4)_2$ in the electrodeposited H-3 thin film.

To further elaborate the composite formation, transmission electron microscopy (TEM) studies were done for the H-3 hybrid sample. Figures 5(A) and 5(B) show the low-magnification TEM images of H-3 hybrid. MXene-intercalated CMP surface is clearly picturized in the low magnification images. Further, fingerprint-like grains are observed in the high-magnification images (Figures 5(C) and 5(D)) due to the saturation of CMP between the MXene particles. Figure 5(E) shows the fast Fourier transform (FFT) profile from the selective region. A derived inverse FFT profile clearly describes the ordered lattice fringes (Figure 5(F)). Figures 5(G) and 5(H) show the phase spectrum with the 0.25 nm and 0.46 nm spacing due to the (30-30) and (0004) lattice planes of CMP and MXene, respectively. The observed results also proved the effective formation of hybrid composite. In addition, TEM elemental mapping studies proved the H-3 composite formation as shown in Figure S4.

The electrochemical performance of pure MXene, CMP, and H-series (H-1, H-2, H-3, H-4, and H-5) electrodes was measured using 6 M KOH aqueous media at room temperature, Hg/HgO being used as a reference electrode in the
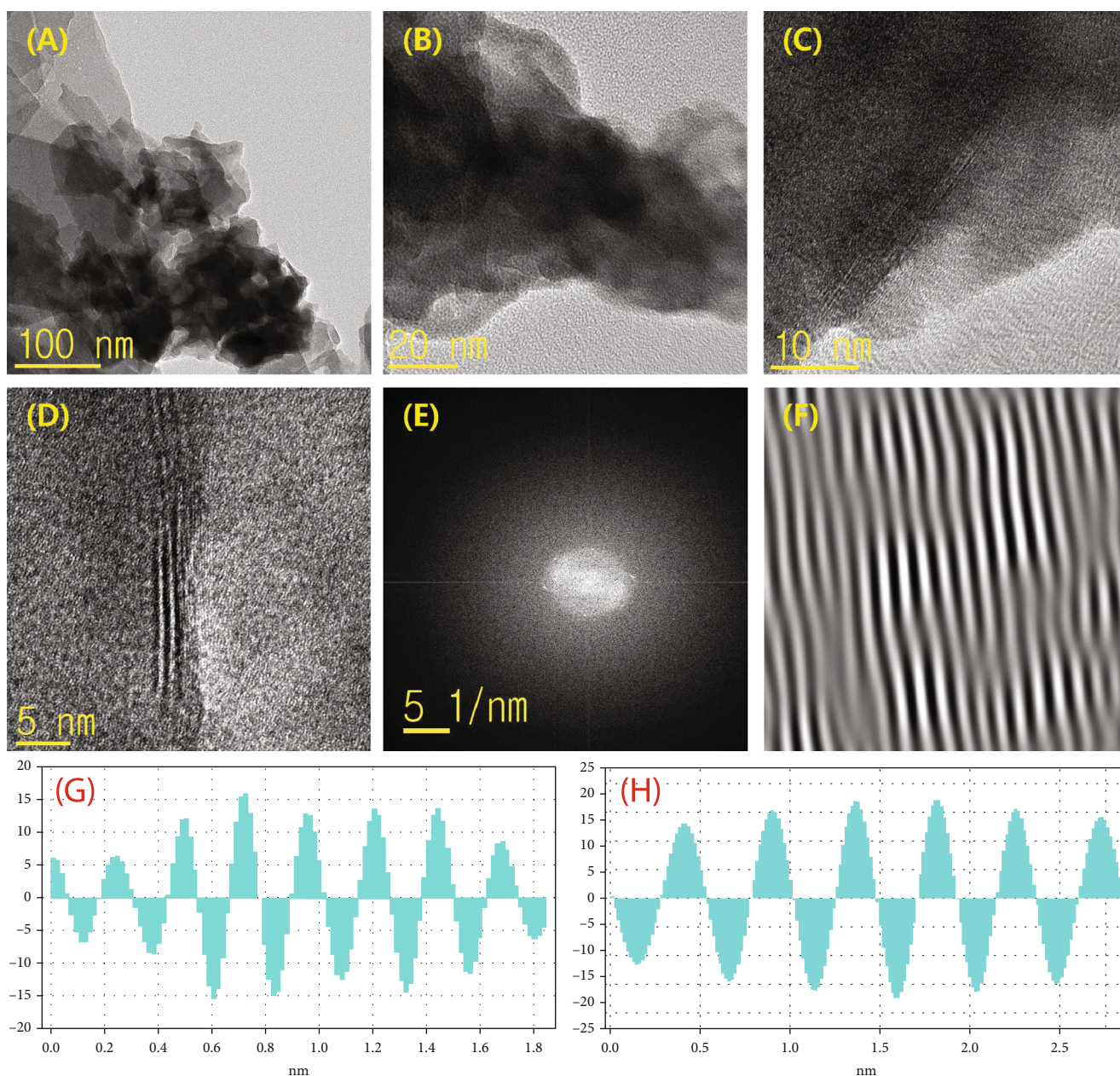
FIGURE 5: TEM images of hybrid H-3 sample: (A–D) different magnification of microscopy images, (E) FFT profile, (F) iFFT profile, and phase spectrum of (G) CMP and (H) MXene.

potential interval of 0–0.5 V. The loading mass of all the samples was around 0.021 mg/cm^2. Figure 6(a) displays the cyclic voltammetry (CV) profiles of the prepared MXene, CMP, and H-series electrodes at a sweep speed of 10 mV·s^{-1}. The observed CV profiles clearly specify the enriched storage behavior of the H-3 electrode compared to other electrodes, and this behavior may be ascribed to the mutual interaction of Mn and Co ions in the storage characteristics of the resulting hybrid. Figure 6(b) spectacles the CV profiles at various sweep rates from 10 to 50 mV·s^{-1} for MXene electrode. The shape of observed CV curve indicates that the prepared MXene electrode exhibited the pseudocapacitive behavior to achieve its storage properties. In addition, the observed CV

profile followed the following intercalation/deintercalation reaction of K$^+$ cations during the charge/discharge process on the layered MXene electrode [43, 44].

$$\mathrm{Ti_3C_2T}_x + x\mathrm{K}^+ + xe^- = \mathrm{K}_x\mathrm{Ti_3C_2T}_x \qquad (1)$$
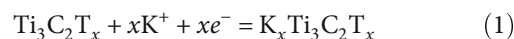
Moreover, the area of the electrode was enriched with an increase in the scanning speed, indicating the high-speed adoptability of fabricated MXene electrode. The shift of oxidation peak towards a negative potential with an enhancement in the scan rate was consistent with an increment in the inner diffusion resistance at high scan speeds. Figure 6(c) shows the CV profiles of the CMP electrode at various scan rates. The
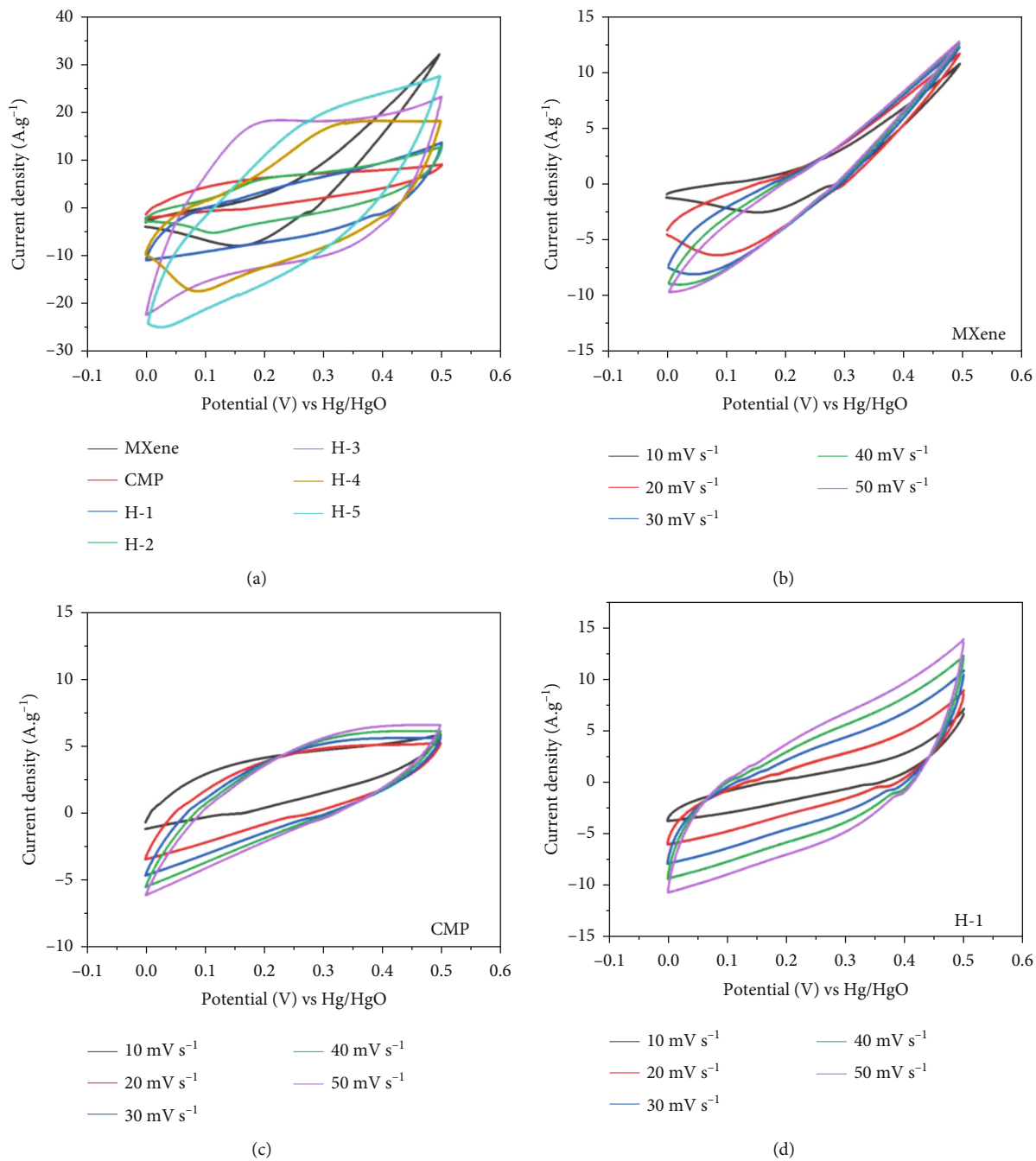
(a)

(b)

(c)

(d)

FIGURE 6: Continued.

(e)

(f)

(g)

(h)
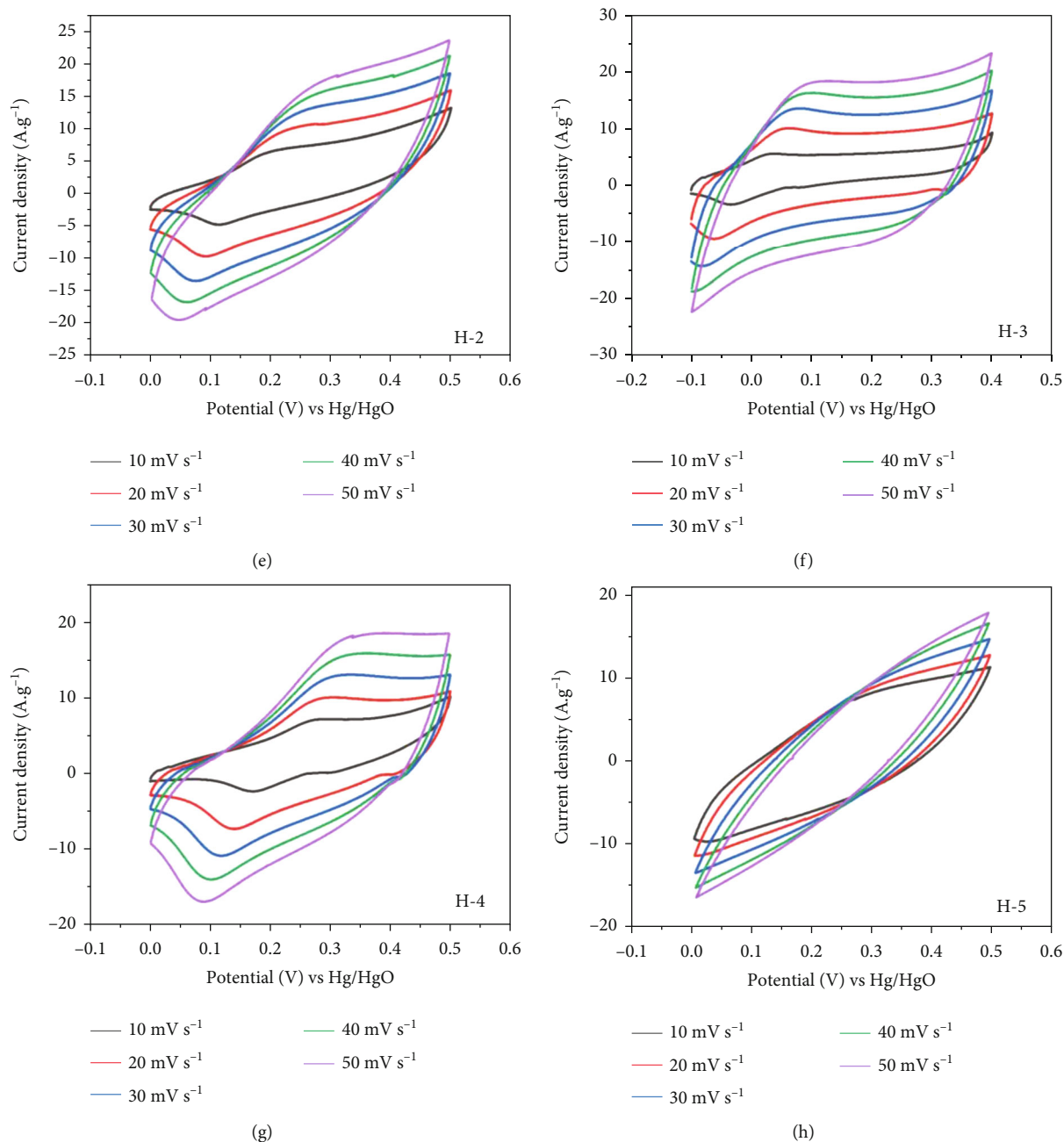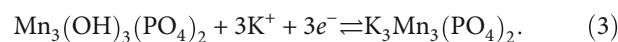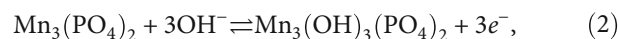
FIGURE 6: Electrochemical measurements: (a) CV profiles of MXene, CMP, and H-series electrodes at a sweep rate of $10 \, mV \cdot s^{-1}$; CV profiles at different scan rates of $10–50 \, mV \cdot s^{-1}$: (b) MXene, (c) CMP, (d) H-1, (e) H-2, (f) H-3, (g) H-4, and (h) H-5.

obtained profiles revealed that the CV curve was highly affected by EDLC characteristics, which could be attributed to the identical composition of Mn and Co atoms in the bimetallic phosphate electrode. In addition, the area of the profile rapidly increased with respect to the scan rate, signifying the high current degree ability of the CMP electrode. Figure 6(d) shows the CV profiles of the H-1 electrode (containing no Co content) at different sweep speeds. The CV profile of the H-1 electrode indicated that the electrode exhibited a strong double-layer capacitive behavior, which could be attributed to the characteristics of the dominant Mn atoms. In addition, the H-1 exhibited EDLC-combined pseudocapacitive transi-

tions (Figure 6(d)), which could be attributed to the intrinsic pseudotype mechanism of $Mn_3(PO_4)_2$ [45, 46].

$$Mn_3(PO_4)_2 + 3OH^- \rightleftharpoons Mn_3(OH)_3(PO_4)_2 + 3e^-, \quad (2)$$

$$Mn_3(OH)_3(PO_4)_2 + 3K^+ + 3e^- \rightleftharpoons K_3Mn_3(PO_4)_2. \quad (3)$$

The CV profile of H-2 electrode at different sweep speeds indicated that it exhibited a blend of pseudo-EDLC characteristics (Figure 6(e)). In addition, the CV profile of the H-2 electrode revealed an asymmetrical shape, which could be attributed to the partial inclusion of Co atoms into Mn to form
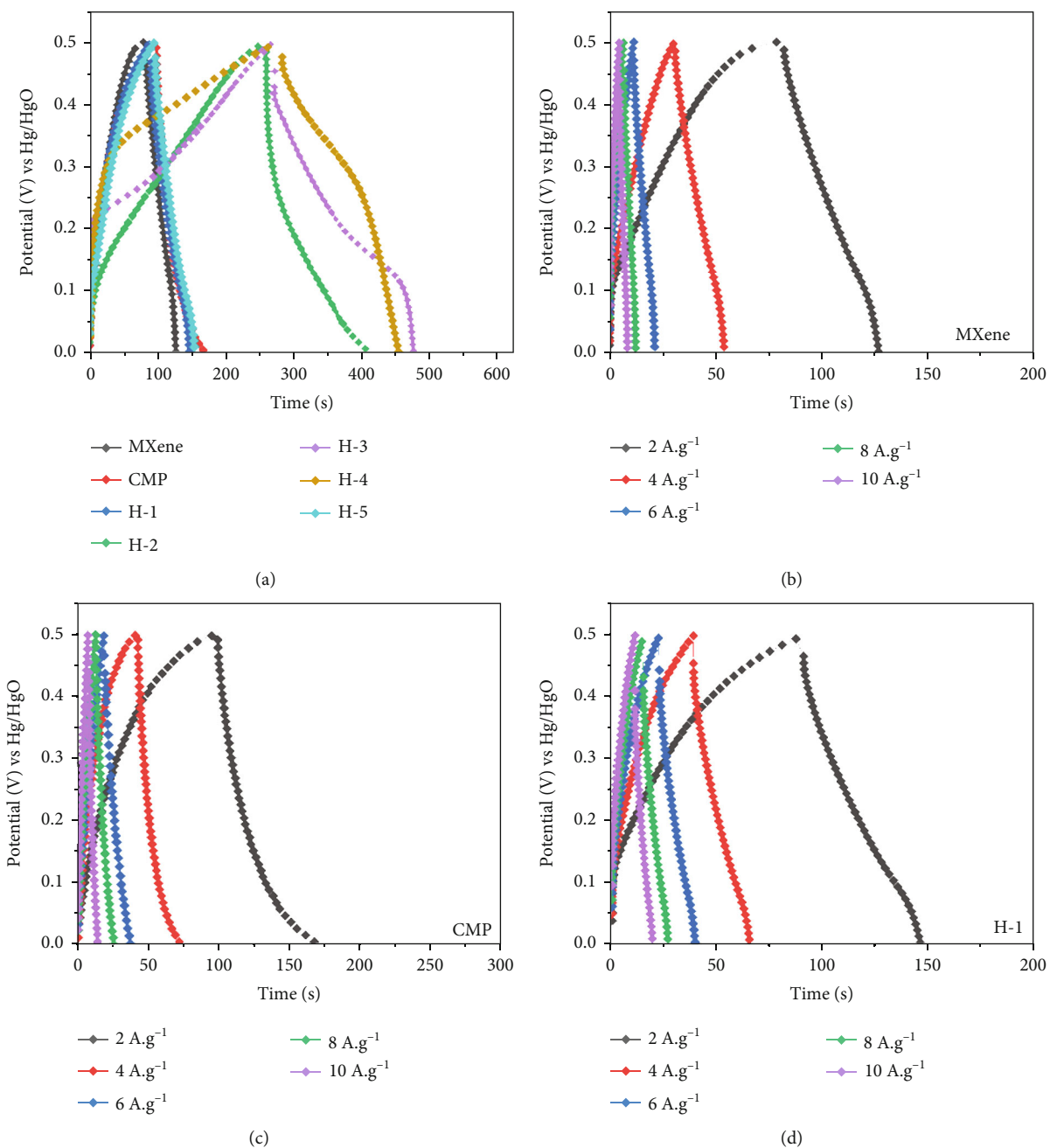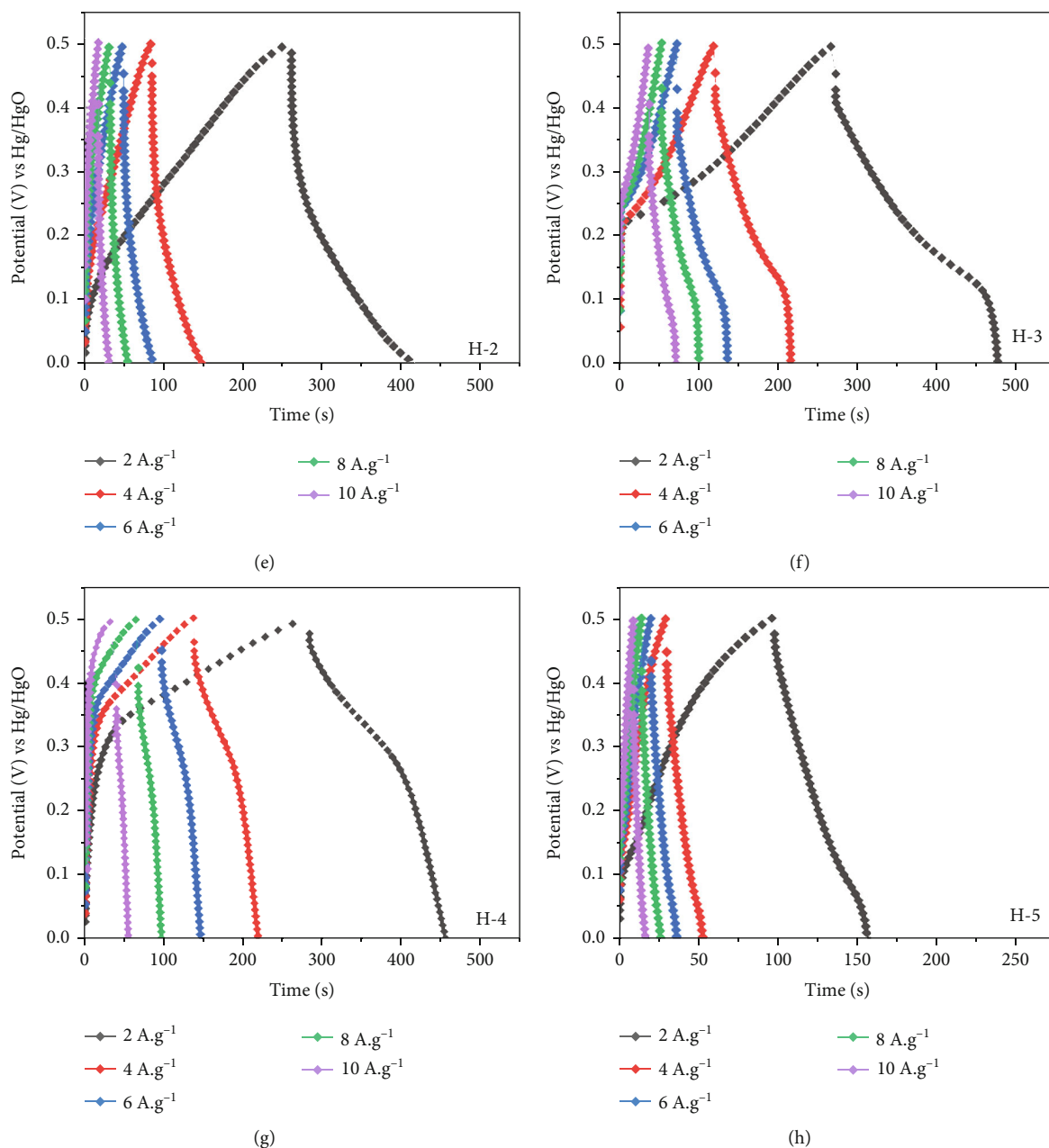
(a)

(b)

(c)

(d)

Figure 7: Continued.

FIGURE 7: GCDs of MXene, CMP, and H-series electrodes at an applied current of 2 A·g⁻¹; GCD profiles at various applied currents (2–10 A·g⁻¹): (b) MXene, (c) CMP, (d) H-1, (e) H-2, (f) H-3, (g) H-4, and (h) H-5.

the bimetallic phosphate on the MXene. Particularly, this irregular shape could be attributed to the dominant pseudocapacitive nature of Mn and the intercalation/deintercalation behavior of Co surface. The introduction of Co metal enabled the transition between the different states of Co^{3+} and Co^{2+} via the reaction kinetics with the alkaline metal in H-2 [47].

$$Co_3(OH)_3(PO_4)_2 + xK^+ + xe^- \rightleftharpoons K_xCo_3(PO_4)_2 \qquad (4)$$
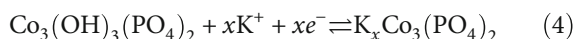
The CV profiles of H-3 electrode showed a larger integrated area associated to the other electrodes, demonstrating the superior charge storage characteristics of the electrode induced by the equicomposition of Mn : Co binary metal with

a combination of phosphates in the MXene hybrid structure. Figure 6(f) shows the CV profiles of H-3 electrode at various sweep rates (10-50 mV·s⁻¹). The results revealed that the charge storage characteristics of H-3 electrode were dominated by the EDLC nature. This can be attributed to the fact that the substitution of equal stoichiometric composition of Co : Mn modified the electronic structure of the hybrid, facilitated electron/ion transport paths, and generated larger active interfacial sites, thus boosting the conductivity and reactivity of the electrode. Similarly, the CVs (Figure 6(g)) of H-4 exhibited an almost rectangular shape owing to the higher content of Co in the resulting material. The periodic improvement with an increment in the sweep rate confirmed the high-rate
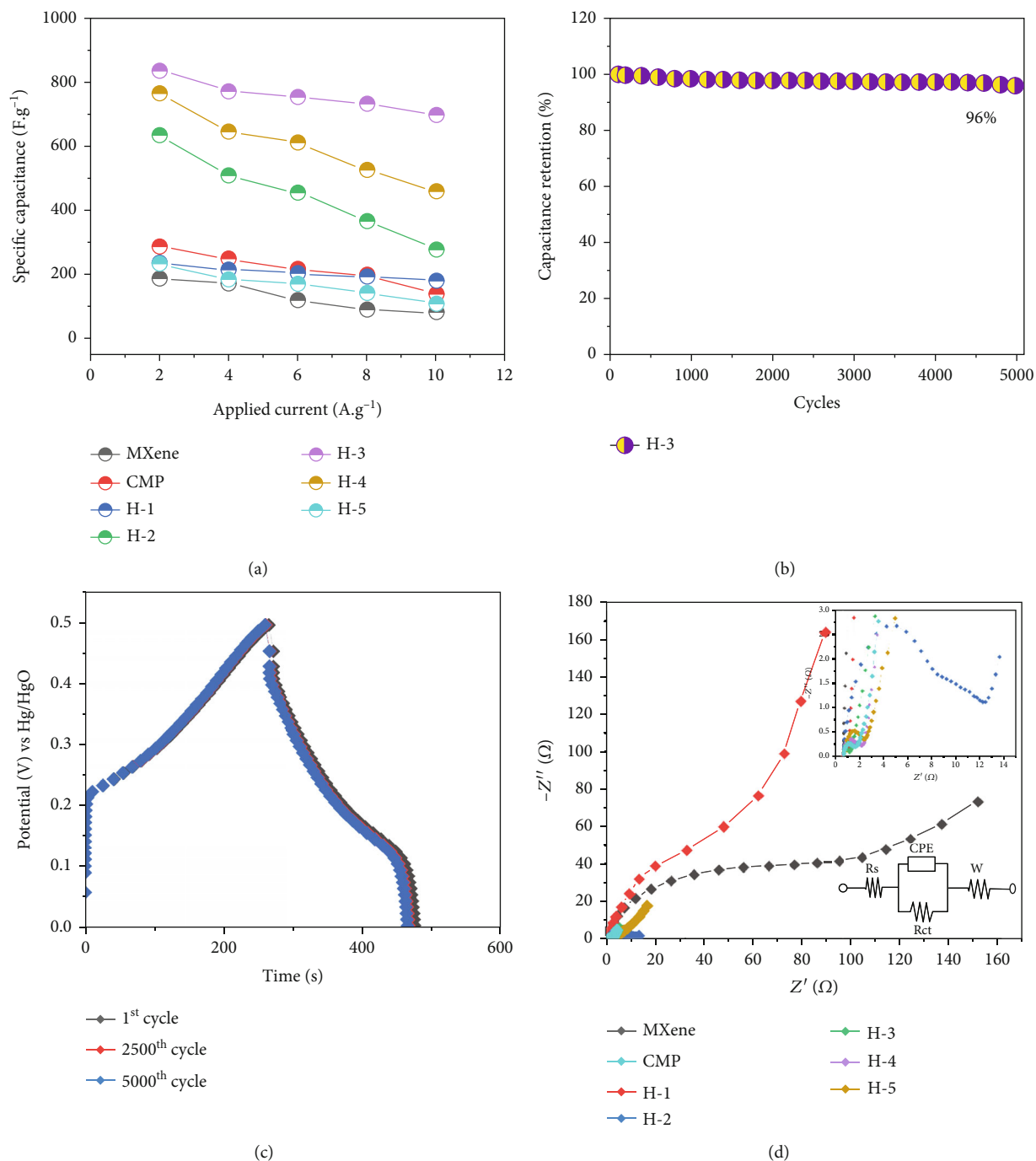
(a)

(b)

(c)

(d)

FIGURE 8: (a) Specific capacities of MXene, CMP, and H-series electrodes at different applied currents; (b) capacitance retention profiles of the H-3 electrode after 5000 GCD cycles; (c) 1st, 2500th, and 5000th GCD profile of the H-3 electrode; (d) the Nyquist profiles of the MXene, CMP, and H-3 series electrodes with an inset showing the equivalent circuit.

ability of the prepared H-4 electrode. The H-5 electrode containing no Mn demonstrated a quasirectangular CV profile shape at diverse sweep rates (Figure 6(h)). The CV results indicate the importance of bimetallic phosphate in the hybrid structure for achieving an efficient supercapacitor behavior.

To evaluate storage characteristics of the MXene, CMP, and H-series (H-1, H-2, H-3, H-4, and H-5) electrodes, galvanostatic charge–discharge (GCD) analysis was achieved at

diverse applied currents in the interval of 0 to 0.5 V vs. Hg/HgO. Figure 7(a) displays the GCD profiles of MXene, CMP, and H-series electrodes at an applied current of 2 A·g⁻¹. Figures 7(b)–7(h) show the GCD profiles of MXene, CMP, and H-1, H-2, H-3, H-4, and H-5 electrodes at the various applied currents, respectively. The outcomes exposed that the assembled electrodes unveiled the typical quasitriangular (nonlinear) GCD profiles owing to a blend of EDLC and
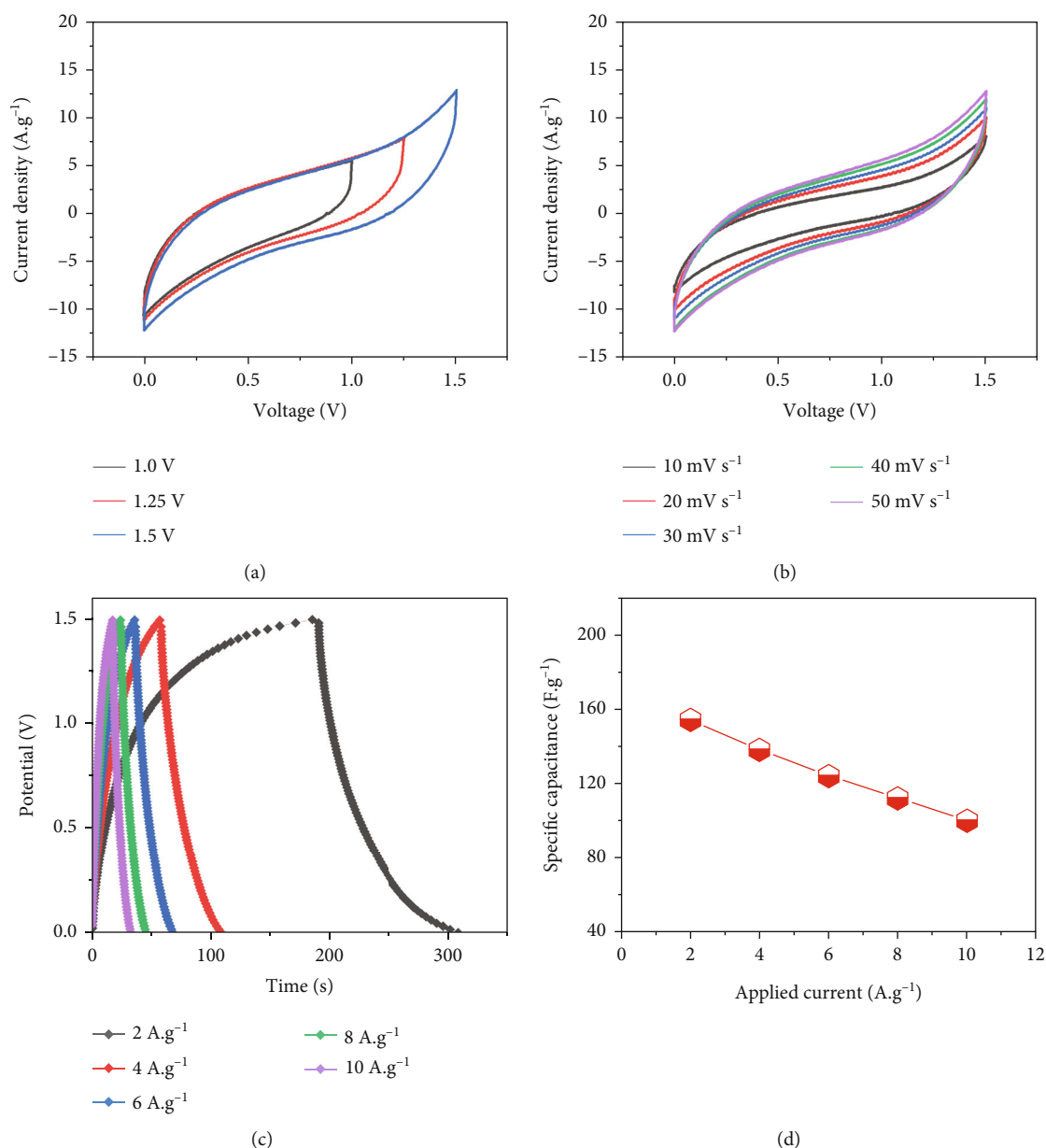
FIGURE 9: (a) CV profiles of symmetric device based on the H-3 electrode at different potential windows; (b) CV profiles at various scan rates (5–50 mV·s^{-1}); (c) GCD plots of the H-3 symmetric device at the different applied currents and (d) their specific capacities.

pseudocapacitive characteristic, as discussed previously [39]. To evaluate the specific capacitance (C) values of all the prepared electrodes, the following equation was used [3, 48]:

$$C\left(\text{Fg}^{-1}\right) = \frac{I(\Delta t)}{m(\Delta V)}, \tag{5}$$

where I is the current density, m is the mass of electroactive materials, ΔV is the potential window, and Δt is the discharge duration.

Figure 8(a) displays the specific capacitance of prepared MXene, CMP, and H-series electrodes at the diverse applied currents. The results revealed that the H-3 electrode showed higher specific capacitance compared to other electrodes.

The H-3 electrode exhibited a high capacitance of 840 F·g^{-1} at an applied current of 2 A·g^{-1}, which was higher than those of the other electrodes, including pure MXene (188 F·g^{-1}), CMP (288 F·g^{-1}), H-1 (236 F·g^{-1}), H-2 (636 F·g^{-1}), H-4 (768 F·g^{-1}), and H-5 (234 F·g^{-1}). The high C values of the H-3 electrode could be credited to the maximum interfacial relation contribution of the two metals (Co and Mn) in the bimetallic phosphate with MXene. At an applied current of 2, 4, 6, 8, and 10 A·g^{-1}, the specific capacities of pure MXene electrode were 188, 172, 120, 90, and 80 F·g^{-1}, respectively, whereas those of the CMP electrode were 288, 248, 216, 195, and 140 F·g^{-1}, respectively. The specific capacitance of the H-1 electrode, which was prepared without Co source, reached 236, 216, 204, 192, and 180 F·g^{-1} at 2, 4, 6, 8, and 10 A·g^{-1}, respectively. After the introduction of Co, which
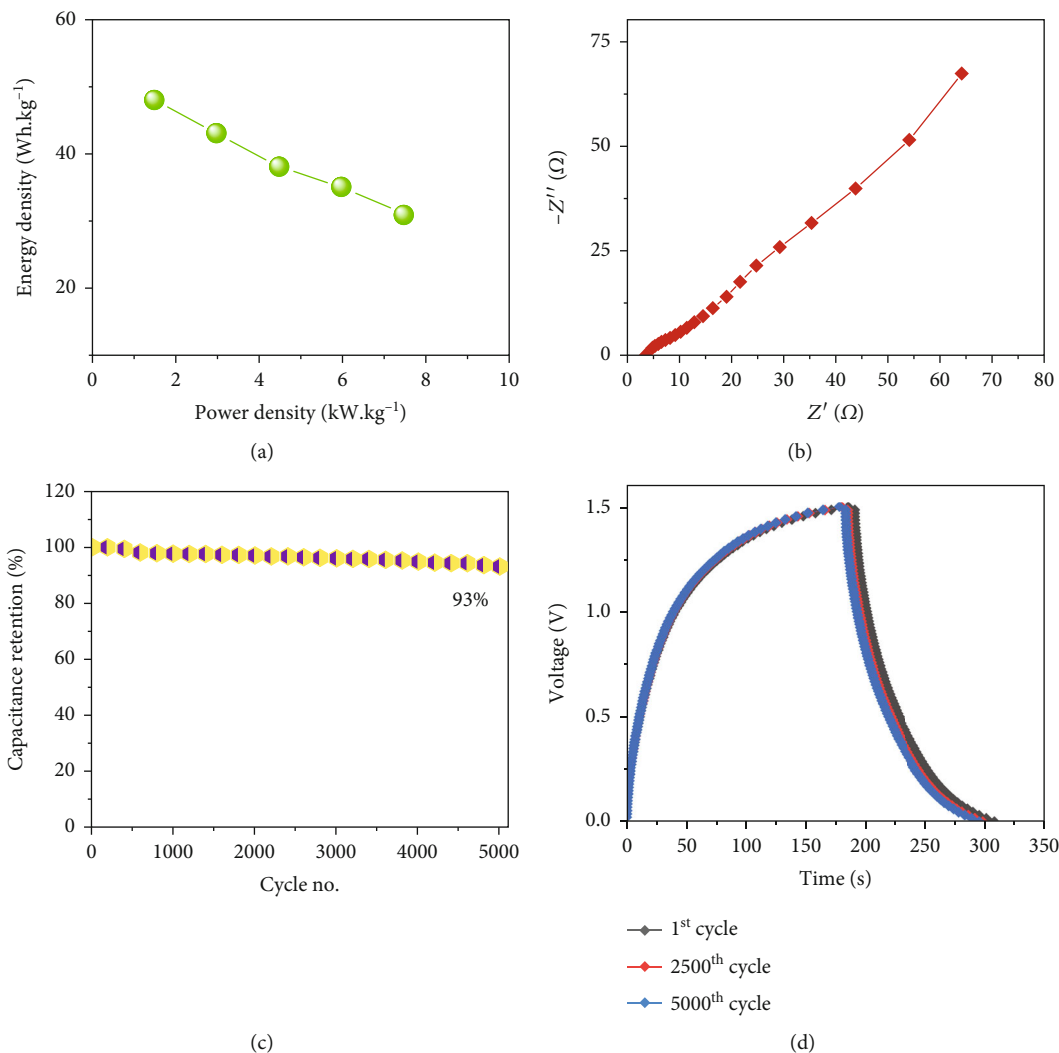
FIGURE 10: (a) Ragone and (b) Nyquist plots of the H-3 symmetric device; (c) capacitance retention profiles after 5000 GCD cycles; (d) assembled symmetric device GCD at 1st, 2500th, and 5000th cycle.

partially replaced Mn atoms (i.e., H-2), the specific capacities of the electrodes at 2, 4, 6, 8, and 10 A·g^{-1} were 636, 512, 456, 368, and 280 F·g^{-1}, respectively. The H-3 electrode achieved the maximum storage behavior with specific capacities of 840, 776, 754, 736, and 700 F·g^{-1} at 2, 4, 6, 8, and 10 A·g^{-1}, respectively, which can be attributed to the equal amount of Mn and Co in the ensuing hybrid material. The H-4 (768, 648, 612, 528, and 460 F·g^{-1} at 2-10 A·g^{-1}, respectively) and H-5 (234, 184, 172, 151, and 110 F·g^{-1} at 2-10 A·g^{-1}, respectively) electrodes exhibited deteriorated capacitance behaviors. The specific capacitance results strongly indicate the importance of the combination of bimetallic phosphate with MXene sheets. The increase in the charge stowage features of the H-3 electrode was accredited to the following factors: (i) high conducting behavior of the electrode owing to the binder-free development on the CC network with the strong adherence properties, which facilitated the proton diffusion and electron/ion transfer from the MXene sheet current collector to the abundant attachment sites of CMP active materials and maintained the long-term structural stability during supercapacitor applications; (ii) the synergistic

effect among Co, Mn, Ti, and P facilitated the intermetallic electron transition which decreased the ion transfer resistance and enhanced the electron transfer rate without impairing ion transport; and (iii) improved conductivity due to the hybridization of CMP with MXene, which also expanded the active material/electrolyte contact to boost the efficiency of active material consumption.

The durability of optimized H-3 electrode was estimated by performing consecutive GCD test at 10 A·g^{-1}. Figure 8(b) displays the initial, 2500th, and 5000th GCD curves of the H-3 electrode. There were no significant changes in the resulting GCD profiles of the H-3 electrode owing to its robust charge storage characteristics (Figure 8(c)). After 5000 cycles, the H-3 electrode maintained 96% of its initial specific capacitance, indicating its improved interfacing surface characteristics and strong interaction with CC skeleton, which enhanced the ion/electron transfer. Electrochemical impedance spectroscopy (EIS) measurements were done throughout to ascertain the electrical conductivity and ionic transport properties of all the electrode materials. The Nyquist plots of all the electrodes confirmed that the H-3

electrode exhibited the smallest curve diameter and charge-transport resistance (R_{ct}) compared to the other electrodes (Figure 8(d)). The fitted electrical circuit relevant to the observed EIS profiles is given in the inset in Figure 8(d) (bottom). The inset in Figure 8(d) (top) shows the zoom-in part of the high-frequency region. The R_{ct} values of the electrodes were observed to increase in the following order: H $-$ 3 ($R_{ct} = 1.7\,\Omega$) < H $-$ 4 ($R_{ct} = 2.8\,\Omega$) < CMP ($R_{ct} = 2.1\,\Omega$) < H $-$ 5 ($R_{ct} = 3.2\,\Omega$) < H $-$ 2 ($R_{ct} = 12.6\,\Omega$) < H $-$ 1 ($R_{ct} = 80.8\,\Omega$) < MXene ($R_{ct} = 120.2\,\Omega$). Compared to H-3, CMP exhibited a swift conducting behavior, which is possible to support the lower R_{ct} value for the optimized sample of H-3 hybrid electrode. The obtained R_{ct} and R_s values of all electrodes are presented in Table S3.

To validate the observed charge stowage characteristics of the H-3 electrode, a symmetric capacitor was assembled engaging the optimized H-3 sample as both positive and negative electrodes with a 6 M KOH electrolyte-soaked Whatman paper. Figure 9(a) displays the CV profiles of the H-3 electrode at different voltage intervals at a sweep speed of 50 mV·s^{-1} from 1.0 to 1.5 V. The CV curve of the electrode at different potential windows exhibited a quasirectangular shape. Figure 9(b) shows the CV profile of the electrode at diverse sweep rates from 10 to 50 mV·s^{-1} at a potential interval of 1.5 V. The CV profile indicated that the prepared H-3 electrode exhibited a high-rate capability. Figure 9(c) displays the GCD profiles of the prepared symmetric device with H-3 electrode at an interval of 1.5 V using different applied currents. The estimated symmetric specific capacities of the H-3 electrodes at applied currents of 2, 4, 6, 8, and 10 A·g^{-1} were 154, 138, 124, 112, and 100 F·g^{-1}, respectively (Figure 9(d)).

Additionally, the power density and energy density values were estimated as the defined relations in the supporting information engaging the obtained specific capacitance values. Figure 10(a) spectacles the Ragone plot of the H-3-based symmetric supercapacitors. The fabricated symmetric supercapacitor exhibited the 48 Wh·kg^{-1} of maximum energy density at 1.5 kW·kg^{-1} power density and sustained an energy density of 31 Wh·kg^{-1} at a high-power density of 7.5 kW·kg^{-1}, indicating its potential application for the energy storage assemblies. These results are superior to the various reported devices, such as NiCo$_2$O$_4$/NiCoP//AC (35.5 Wh·kg^{-1} at 750.4 W·kg^{-1}) [49], P-CSs@Ni$_1$-Co$_2$-P NSs//AC (16.5 Wh·kg^{-1} at 750 W·kg^{-1}) [50], O-NiCoP@rGO//AC (21 Wh·kg^{-1} at 775 W·kg^{-1}) [51], P-Co$_2$MnO$_{4-x}$//AC (25.18 Wh·kg^{-1} at 800.07 W·kg^{-1}) [52], and Mn-CoP//AC (35.21 Wh·kg^{-1} at 193 W·kg^{-1}) [53]. The detailed comparison of the device performance to those described in the literature is given in Table S4. Figure 10(b) displays the Nyquist plot of the symmetric device assembled with H-3 electrode. The device exhibited R_s and R_{ct} values of 3.5 and 20.5 Ω, respectively. To evaluate the stability of symmetric device based on H-3, GCD was performed for 5000 cycles. The assembled H-3-based symmetric capacitor device retained 93% of its primary capacitance after 5000 cycles, signifying the excellent constancy of the as-prepared supercapacitor (Figure 10(c)). Figure 10(d) exposes the GCD profiles of the device at the initial, 2500th, and 5000th cycles.

The performance of assembled symmetric capacitor degraded slightly after the 2500th cycle, which may be credited to increased internal resistance between grains and the destruction of surface porosity by the electrolyte ion diffusion [54]. The initial loss in the specific capacitance can be caused by the loss of surface active sites on the electrode.

4. Conclusion

This study elaborated the direct and binder-free synthesis of MXene-CMP films on a highly conductive CC substrate via electrodeposition to achieve efficient supercapacitors. The results established the occurrence of the bimetal ions (Co and Mn) deposited in the prepared thin films via electrodeposition. In addition, FESEM, the Raman, XRD, and EDS results strongly confirmed the different composition of Co$_x$Mn$_{3-x}$(PO$_4$)$_2$ and MXene in the thin films. The electrochemical results demonstrated that the H-3 film achieved the maximum specific capacitance of 840 F·g^{-1} at a 2 A·g^{-1} current density and retained a high capacitive retention of 96% after 5000 GCD cycles. The assembled symmetric device displayed a 154 F·g^{-1} specific capacitance at 2 A·g^{-1} current density and an energy density of 48 Wh·kg^{-1} at 1.5 kW·kg^{-1} power density. Hence, this work presents a novel method to design binder-free, highly active binary metal CMP-incorporated MXene electrode for efficient energy storage devices.

Data Availability

Data is available on request.

Conflicts of Interest

The authors declare that they have no known competing financial interests or personal relationships that could have appeared to influence the work reported in this paper.

Acknowledgments

Supplementary Materials

The detailed electrochemical and analytical characterization information is provided. Surface, structural, and compositional analyses of MXene sample are provided. Elemental composition of H-3 sample is provided. The obtained electrochemical parameter values and their extended comparison with the reported literatures are tabulated. (Supplementary Materials)

References

[1] S. Hussain, D. Vikraman, Z. Ali Sheikh et al., "WS$_2$-embedded MXene/GO hybrid nanosheets as electrodes for asymmetric supercapacitors and hydrogen evolution reactions," *Chemical Engineering Journal*, vol. 452, article 139523, 2023.

[2] G. Nagaraju, S. C. Sekhar, B. Ramulu, and J. S. Yu, "High-performance hybrid supercapacitors based on MOF-derived hollow ternary chalcogenides," *Energy Storage Materials*, vol. 35, pp. 750–760, 2021.

[3] D. Vikraman, S. Hussain, I. Rabani et al., "Engineering MoTe$_2$ and Janus SeMoTe nanosheet structures: first-principles roadmap and practical uses in hydrogen evolution reactions and symmetric supercapacitors," *Nano Energy*, vol. 87, article 106161, 2021.

[4] R. Brooke, J. Åhlin, K. Hübscher et al., "Large-scale paper supercapacitors on demand," *Journal of Energy Storage*, vol. 50, article 104191, 2022.

[5] S. Satpathy, N. K. Misra, D. K. Shukla, V. Goyal, B. K. Bhattacharyya, and C. S. Yadav, "An in-depth study of the electrical characterization of supercapacitors for recent trends in energy storage system," *Journal of Energy Storage*, vol. 57, article 106198, 2023.

[6] T. Kshetri, D. T. Tran, H. T. Le et al., "Recent advances in MXene-based nanocomposites for electrochemical energy storage applications," *Progress in Materials Science*, vol. 117, article 100733, 2021.

[7] S. Mukherjee, Z. Ren, and G. Singh, "Beyond graphene anode materials for emerging metal ion batteries and supercapacitors," *Nano-Micro Letters*, vol. 10, pp. 1–27, 2018.

[8] D. Vikraman, S. Hussain, L. Hailiang et al., "Spinel-structured metal oxide-embedded MXene nanocomposites for efficient water splitting reactions," *Inorganic Chemistry Frontiers*, vol. 9, no. 22, pp. 5903–5916, 2022.

[9] S. Hussain, D. Vikraman, M. Sarfraz et al., "Design of XS$_2$ (X = W or Mo)-decorated VS$_2$ hybrid nano-architectures with abundant active edge sites for high-rate asymmetric supercapacitors and hydrogen evolution reactions," *Small*, vol. 19, article 2205881, 2022.

[10] D. Vikraman, S. Hussain, K. Karuppasamy et al., "Engineering the novel MoSe$_2$-Mo$_2$C hybrid nanoarray electrodes for energy storage and water splitting applications," *Applied Catalysis B: Environmental*, vol. 264, article 118531, 2020.

[11] S. Hussain, I. Rabani, D. Vikraman et al., "Hybrid design using carbon nanotubes decorated with Mo$_2$C and W$_2$C nanoparticles for supercapacitors and hydrogen evolution reactions," *ACS Sustainable Chemistry & Engineering*, vol. 8, no. 32, pp. 12248–12259, 2020.

[12] S. Hussain, I. Rabani, D. Vikraman et al., "MoS$_2$@ X$_2$C (X= Mo or W) hybrids for enhanced supercapacitor and hydrogen evolution performances," *Chemical Engineering Journal*, vol. 421, article 127843, 2021.

[13] C. Hao, Y. Wu, Y. An et al., "Interface-coupling of CoFe-LDH on MXene as high-performance oxygen evolution catalyst," *Materials Today Energy*, vol. 12, pp. 453–462, 2019.

[14] H. Jiang, Z. Wang, Q. Yang et al., "A novel MnO$_2$/Ti$_3$C$_2$Tx MXene nanocomposite as high performance electrode materials for flexible supercapacitors," *Electrochimica Acta*, vol. 290, pp. 695–703, 2018.

[15] M. Alrwashdeh and S. A. Alameri, "SiC and FeCrAl as potential cladding materials for APR-1400 neutronic analysis," *Energies*, vol. 15, no. 10, p. 3772, 2022.

[16] M. Naguib, M. W. Barsoum, and Y. Gogotsi, "Ten years of progress in the synthesis and development of MXenes," *Advanced Materials*, vol. 33, no. 39, article e2103393, 2021.

[17] Y. Gogotsi and B. Anasori, "The rise of MXenes," *ACS Nano*, vol. 13, no. 8, pp. 8491–8494, 2019.

[18] C. Ji, H. Cui, H. Mi, and S. Yang, "Applications of 2D MXenes for electrochemical energy conversion and storage," *Energies*, vol. 14, no. 23, p. 8183, 2021.

[19] A. A. Mirghni, K. O. Oyedotun, B. A. Mahmoud, O. Fasakin, D. J. Tarimo, and N. Manyala, "A study of Co-Mn phosphate supported with graphene foam as promising electrode materials for future electrochemical capacitors," *International Journal of Energy Research*, vol. 46, no. 3, pp. 3080–3094, 2022.

[20] L. Feng and H. Xue, "Advances in transition-metal phosphide applications in electrochemical energy storage and catalysis," *ChemElectroChem*, vol. 4, no. 1, pp. 20–34, 2017.

[21] A. Numan, J. Iqbal, P. Jagadish et al., "Tailoring crystallinity of 2D cobalt phosphate to introduce pseudocapacitive behavior," *Journal of Energy Storage*, vol. 54, article 105371, 2022.

[22] N. Zhang, Y. Li, J. Xu et al., "High-performance flexible solid-state asymmetric supercapacitors based on bimetallic transition metal phosphide nanocrystals," *ACS Nano*, vol. 13, no. 9, pp. 10612–10621, 2019.

[23] F. S. Omar, A. Numan, N. Duraisamy, M. M. Ramly, K. Ramesh, and S. Ramesh, "Binary composite of polyaniline/copper cobaltite for high performance asymmetric supercapacitor application," *Electrochimica Acta*, vol. 227, pp. 41–48, 2017.

[24] Y. Zhou, C. Liu, X. Li et al., "Chemical precipitation synthesis of porous Ni$_2$P$_2$O$_7$ nanowires for supercapacitor," *Journal of Alloys and Compounds*, vol. 790, pp. 36–41, 2019.

[25] Y.-H. Dai, L.-B. Kong, K. Yan, M. Shi, Y.-C. Luo, and L. Kang, "Facile fabrication of manganese phosphate nanosheets for supercapacitor applications," *Ionics*, vol. 22, no. 8, pp. 1461–1469, 2016.

[26] P. K. Katkar, S. J. Marje, S. S. Pujari, S. A. Khalate, A. C. Lokhande, and U. M. Patil, "Enhanced energy density of all-solid-state asymmetric supercapacitors based on morphologically tuned hydrous cobalt phosphate electrode as cathode material," *ACS Sustainable Chemistry & Engineering*, vol. 7, no. 13, pp. 11205–11218, 2019.

[27] M. Alzaid, M. Z. Iqbal, S. Siddique, and N. M. A. Hadia, "Exploring the electrochemical performance of copper-doped cobalt–manganese phosphates for potential supercapattery applications," *RSC Advances*, vol. 11, no. 45, pp. 28042–28051, 2021.

[28] E. M. Ibrahim, M. M. Hasan, A. A. Saleh, and N. K. Allam, "Structural engineering of Ti-Mn bimetallic phosphide nanotubes for efficient photoelectrochemical water splitting," *International Journal of Hydrogen Energy*, vol. 46, no. 5, pp. 3605–3614, 2021.

[29] C. C. Lee, F. S. Omar, A. Numan, N. Duraisamy, K. Ramesh, and S. Ramesh, "An enhanced performance of hybrid supercapacitor based on polyaniline-manganese phosphate binary composite," *Journal of Solid State Electrochemistry*, vol. 21, no. 11, pp. 3205–3213, 2017.

[30] S. Hussain, D. Vikraman, M. T. Mehran et al., "Ultrasonically derived WSe$_2$ nanostructure embedded MXene hybrid composites for supercapacitors and hydrogen evolution reactions," *Renewable Energy*, vol. 185, pp. 585–597, 2022.

[31] S. Hussain, H. Liu, M. Hussain et al., "Development of MXene/WO$_3$ embedded PEDOT: PSS hole transport layers for highly efficient perovskite solar cells and X-ray detectors," *International Journal of Energy Research*, vol. 46, no. 9, pp. 12485–12497, 2022.

[32] S. Hussain, I. Rabani, D. Vikraman et al., "Designing the MXene/molybdenum diselenide hybrid nanostructures for

high-performance symmetric supercapacitor and hydrogen evolution applications," *International Journal of Energy Research*, vol. 45, no. 13, pp. 18770–18785, 2021.

[33] G. Penel, G. Leroy, C. Rey, and E. Bres, "MicroRaman spectral study of the PO_4 and CO_3 vibrational modes in synthetic and biological apatites," *Calcified Tissue International*, vol. 63, no. 6, pp. 475–481, 1998.

[34] V. Kitenge, K. Oyedotun, O. Fasakin et al., "Enhancing the electrochemical properties of a nickel–cobalt-manganese ternary hydroxide electrode using graphene foam for supercapacitors applications," *Materials for Renewable and Sustainable Energy*, vol. 10, pp. 1–16, 2021.

[35] P. Legutko, J. Pęza, A. Villar Rossi et al., "Elucidation of unexpectedly weak catalytic effect of doping with cobalt of the cryptomelane and birnessite systems active in soot combustion," *Topics in Catalysis*, vol. 62, no. 7-11, pp. 599–610, 2019.

[36] A. Pazniak, P. Bazhin, N. Shplis et al., "Ti3C2Tx MXene characterization produced from SHS-ground Ti3AlC2," *Materials & Design*, vol. 183, article 108143, 2019.

[37] V. V. Atuchin, V. G. Kesler, N. V. Pervukhina, and Z. Zhang, "Ti 2p and O 1s core levels and chemical bonding in titanium-bearing oxides," *Journal of Electron Spectroscopy and Related Phenomena*, vol. 152, no. 1-2, pp. 18–24, 2006.

[38] P. W. Menezes, A. Indra, V. Gutkin, and M. Driess, "Boosting electrochemical water oxidation through replacement of O_h Co sites in cobalt oxide spinel with manganese," *Chemical Communications*, vol. 53, no. 57, pp. 8018–8021, 2017.

[39] P. K. Katkar, S. J. Marje, V. G. Parale et al., "Fabrication of a high-performance hybrid supercapacitor based on hydrothermally synthesized highly stable cobalt manganese phosphate thin films," *Langmuir*, vol. 37, no. 17, pp. 5260–5274, 2021.

[40] A. E. Elkholy, F. E.-T. Heakal, and N. K. Allam, "A facile electrosynthesis approach of amorphous Mn-Co-Fe ternary hydroxides as binder-free active electrode materials for high-performance supercapacitors," *Electrochimica Acta*, vol. 296, pp. 59–68, 2019.

[41] D. Vikraman, H. J. Park, S.-I. Kim, and M. Thaiyan, "Magnetic, structural and optical behavior of cupric oxide layers for solar cells," *Journal of Alloys and Compounds*, vol. 686, pp. 616–627, 2016.

[42] S. Hussain, D. Vikraman, G. Nazir et al., "Development of binder-free three-dimensional honeycomb-like porous ternary layered double hydroxide-embedded MXene sheets for bifunctional overall water splitting reactions," *Nanomaterials*, vol. 12, no. 16, p. 2886, 2022.

[43] W. Wu, D. Niu, J. Zhu et al., "Hierarchical architecture of Ti_3C_2@PDA/$NiCo_2S_4$ composite electrode as high-performance supercapacitors," *Ceramics International*, vol. 45, no. 13, pp. 16261–16269, 2019.

[44] Y. Luo, C. Yang, Y. Tian, Y. Tang, X. Yin, and W. Que, "A long cycle life asymmetric supercapacitor based on advanced nickel-sulfide/titanium carbide (MXene) nanohybrid and MXene electrodes," *Journal of Power Sources*, vol. 450, article 227694, 2020.

[45] C. Yang, L. Dong, Z. Chen, and H. Lu, "High-performance all-solid-state supercapacitor based on the assembly of graphene and manganese(II) phosphate nanosheets," *The Journal of Physical Chemistry C*, vol. 118, no. 33, pp. 18884–18891, 2014.

[46] C. Wu, X. Lu, L. Peng et al., "Two-dimensional vanadyl phosphate ultrathin nanosheets for high energy density and flexible pseudocapacitors," *Nature Communications*, vol. 4, no. 1, p. 2431, 2013.

[47] H. Liang, C. Xia, Q. Jiang, A. N. Gandi, U. Schwingenschlögl, and H. N. Alshareef, "Low temperature synthesis of ternary metal phosphides using plasma for asymmetric supercapacitors," *Nano Energy*, vol. 35, pp. 331–340, 2017.

[48] T. Sun, Z. Li, X. Liu, L. Ma, J. Wang, and S. Yang, "Facile construction of 3D graphene/MoS_2 composites as advanced electrode materials for supercapacitors," *Journal of Power Sources*, vol. 331, pp. 180–188, 2016.

[49] Q. Zong, H. Yang, Q. Wang et al., "$NiCo_2O_4$/NiCoP nanoflake-nanowire arrays: a homogeneous hetero-structure for high performance asymmetric hybrid supercapacitors," *Dalton Transactions*, vol. 47, no. 45, pp. 16320–16328, 2018.

[50] T. Dang, L. Wang, D. Wei et al., "Bifunctional phosphorization synthesis of mesoporous networked Ni-Co-P/phosphorus doped carbon for ultra-stable asymmetric supercapacitors," *Electrochimica Acta*, vol. 299, pp. 346–356, 2019.

[51] Y. Zhang, L. Sun, L. Zhang et al., "Highly porous oxygen-doped NiCoP immobilized in reduced graphene oxide for supercapacitive energy storage," *Composites Part B: Engineering*, vol. 182, article 107611, 2020.

[52] F. Xiang, X. Zhou, X. Yue, Q. Hu, Q. Zheng, and D. Lin, "An oxygen-deficient cobalt-manganese oxide nanowire doped with P designed for high performance asymmetric supercapacitor," *Electrochimica Acta*, vol. 379, article 138178, 2021.

[53] G. Zhu, L. Yang, W. Wang et al., "Hierarchical three-dimensional manganese doped cobalt phosphide nanowire decorated nanosheet cluster arrays for high-performance electrochemical pseudocapacitor electrodes," *Chemical Communications*, vol. 54, no. 66, pp. 9234–9237, 2018.

[54] A. Winchester, S. Ghosh, S. Feng et al., "Electrochemical characterization of liquid phase exfoliated two-dimensional layers of molybdenum disulfide," *ACS Applied Materials & Interfaces*, vol. 6, no. 3, pp. 2125–2130, 2014.